Available online at www.sciencedirect.com

ScienceDirect

Cement and Concrete Research 36 (2006) 1556 – 1566

Cement and Concrete Research

# Estimating transport properties of mortars using image analysis on backscattered electron images

H.S. Wong *, N.R. Buenfeld, M.K. Head

*Concrete Durability Group, Department of Civil and Environmental Engineering, Imperial College London, SW7 2AZ, UK*

Received 25 August 2005; accepted 9 May 2006

## Abstract

The pore structure of two ordinary Portland cement mortars at water–cement ratio of 0.35 and 0.70 was characterised using quantitative backscattered electron imaging. The mortars were cured and conditioned to produce a range of pore structure characteristics. Image analysis was used to characterise the pore structure in terms of simple morphological parameters such as resolvable porosity and the specific surface area. These were found to be correlated to measured transport coefficients (diffusivity, permeability and sorptivity), suggesting the feasibility of image analysis to derive valuable quantitative information describing the pore structure that can be used as input values for a transport prediction model. A simple analytical model incorporating tortuosity and constrictivity was used to predict oxygen diffusivity and a variant of the Kozeny–Carman model was used to predict oxygen permeability. The diffusion model tended to over-predict for the lower *w*/*c* ratio mortar, but the general agreement was reasonable, with 90% of the estimated values within a factor of two from the measured values. The modified Kozeny–Carman model, however, over-predicted all permeability values with an error of between half to one order of magnitude.

*Keywords:* Backscattered electron microscopy; Image analysis; Microstructure; SEM; Transport properties; Pore structure

## 1. Introduction

This is an exploratory study of the feasibility of using image analysis on backscattered electron (BSE) images to extract quantitative information on pore structure that can be used to develop simple transport prediction models for cement-based materials. Transport properties govern the rate of all major deterioration processes and the service life of building materials, hence, much effort has been dedicated to their prediction. Experimental methods for investigating pore structure are divided into indirect methods such as mercury intrusion porosimetry (MIP), that rely on measurements of a secondary or derived property, and direct methods such as microscopy, which produces an image of the microstructure that reveals the morphology and spatial relationship of the pores and various phases. Measurements made on a 2D image can, to some extent, be related to the 3D structure via stereology rules [1,2].

Since the rate of mass transport is governed by the interconnected pore space, it follows that the pore parameters derived from microscopy may be used to predict transport properties. Indeed, there are many examples of such work particularly in the field of geological sciences, where research is aimed at understanding the transport of oil and gases, contaminants and solutes in soils and rock formations. However, there are not many examples of similar work on cement-based materials, possibly because of their greater complexity, compounded by limitations in instrumentation. Two examples of studies involving microscopy to predict transport properties of cementitious materials are the recent works by Hu and Stroeven [3], who used BSE imaging to determine the critical pore size to predict permeability via general effective media theory, and Koster et al. [4], who derived water permeability and vapour diffusivity from 3D microtomographic images via network modelling. Both studies were performed on hardened cement pastes. In this contribution, we will attempt to use 2D pore parameters from BSE images to estimate the gaseous diffusivity and permeability coefficients of mortar samples. Mortars were chosen for this preliminary study because they resemble concretes by having sand particles and aggregate–paste

---

* Corresponding author. Tel.: +44 20 7594 5957; fax: +44 20 7225 2716.
*E-mail address:* hong.wong@imperial.ac.uk (H.S. Wong).

0008-8846/$ - see front matter © 2006 Elsevier Ltd. All rights reserved.
doi:10.1016/j.cemconres.2006.05.002

interfaces, but are more homogeneous due to the exclusion of large aggregate particles.

Properties that are relevant to molecular transport are the volume of interconnected pores, surface area of the solid–void interface, pore shape, constrictivity, tortuosity and connectivity of the pores. However, a BSE image is only a 2D representation of a 3D structure. While porosity and surface area are easily obtainable from a 2D section, the shape, connectivity and tortuosity are impossible to define and to measure from a 2D image. Researchers have often relied on other properties, for example the formation factor (the ratio of resistivity of the saturated porous medium to the resistivity of the pore water), to characterise connectivity and tortuosity. 3D imaging such as microtomography and confocal microscopy may provide valuable insights on higher-order parameters like connectivity and tortuosity. However, although such parameters can describe simple pore configurations effectively, their concept is difficult to implement on complex porous media.

The inherent limitation of any imaging technique is the size range that is available for quantitative analysis. This presents two complications: first, the ability to resolve the smallest features present, and second, the size of the field of view necessary to obtain a statistically valid representation of the microstructure. Increasing the magnification can improve the resolving ability up to the resolution limit of a particular imaging system, but a high magnification will result in a small field of view, and hence, a larger number of images must be analysed. A small field of view also limits the size of the largest feature that can be quantified accurately, regardless of the total number of images analysed. One must always remember that such limitations exist when using image analysis for quantitative work.

## 2. Experimental

### 2.1. General considerations

For an investigation of this kind, it is important that the transport mechanisms to be studied do not alter the pore structure during the test itself, hence those that involve prolonged exposure to water, carbon dioxide or chloride ions were deemed unsuitable. Application of high-pressure was avoided to minimise the risk of specimen damage. Although most deterioration processes begin with the movement of the contaminant through the exposed surface, the surface zone is affected by microstructural gradients that can complicate interpretation of test results. Therefore, transport tests were carried out on bulk, rather than surface, material [5]. In this study, specimens were tested sequentially for oxygen diffusion, oxygen permeation and water absorption. This sequence of testing is advantageous because the same specimen can be used for all tests since successive test results are not affected by the previous test. Oxygen transport is relevant in view of its importance to reinforcement corrosion while water ingress via capillary suction is a major transport phenomenon occurring in concrete structures. In the water absorption test, the sorptivity coefficient can be calculated using data obtained from the first few hours of water uptake, thus the effect of further hydration on pore structure during this period is assumed negligible.

The gaseous diffusivity and permeability, and water sorptivity are dependent upon the degree of pore saturation, therefore specimens must be conditioned to a standard moisture state prior to testing so that a meaningful comparison can be made. Conditioning at high humidity may be more practical because less time is required to reach equilibrium. However, a sample conditioned at high humidity contains many saturated pores that are effectively blocked and do not contribute to transport, but may be imaged and analysed during microscopy. In a digital image, pores finer than the resolution limit are not measured and thus, if the conditioning regime can be devised to ensure all pores smaller than this are saturated, then the issue of not accounting for the smaller capillaries does not arise. On the other hand, if the size of the largest saturated pore is greater than the resolution limit, then some of the measured pores from the images actually do not contribute to transport. In short, the largest saturated pore size should match the image resolution, but this is not easy to achieve as there are no reliable means to control the drying process in such a way that ensures this. Also, the drying out process does not necessarily progress evenly from the largest to the smallest capillaries because of ink bottle effects.

Previous work suggests that the influence of pore saturation on the transport properties of cement-based materials is only significant when the internal relative humidity (RH) level is greater than about 60%. Parrott [6] found that the air permeability and water absorption for a range of concretes (*w*/*c*: 0.46, 0.59, 0.72) were very sensitive to the moisture content at RH values above 60%. Ollivier et al. [7] investigated many gas permeability results found in the literature; it was observed that large increases in permeability occurred when drying from saturation down to 75% RH, but further drying to about 40% RH had little effect. Similar observations can be made on experimental data obtained by Galle et al. [8] and Jacobs [9]. These findings suggest that at RH lower than 60%, the increase in transport properties is negligible because most of the pores relevant to transport (capillary pores and microcracks) have already been emptied. Thus, it was decided that specimens for this study should be dried to at least this level in order to minimise the influence of pore saturation. When dried further, the increase in mass transport is only very slight, and is probably partially associated with changes in the pore structure, for example cracking, rather than solely the emptying of the pores [7].

### 2.2. Specimen preparation, curing and conditioning

Ordinary Portland cement and medium graded (BS 882: 1992) siliceous sand were used to prepare two mortar mixtures according to the proportions given in Table 1. The decision to use very high and low *w*/*c* ratio was based on the intention to study samples of a wide range of pore structure characteristics

Table 1
Mixture proportions

| Mixture | Cement (kg/m$^3$) | Sand (kg/m$^3$) | Free *w*/*c* ratio |
|---|---|---|---|
| M 0.7 | 365 | 1635 | 0.70 |
| M 0.35 | 550 | 1635 | 0.35 |

and to determine the limits of applicability and sensitivity of the derived pore structure–transport relationships. The sand volume fraction was 63%. A naphthalene sulphonated type superplasticizer was used for M 0.35 at a dosage of 0.5% by weight of cement. Cylindrical specimens (100 mm$\phi \times 250$ mm) were cast, demoulded after 24 h and sealed cured in cling film at 20 °C. After an initial curing period, each cylinder was sectioned to produce three 50 mm thick discs for transport testing and two 10 mm thick discs for microscopy. Discs of approximately 30 mm thickness from the top and bottom face of each cylinder were discarded.

Several curing and conditioning regimes, shown in Table 2, were applied in order to produce specimens with a range of maturity and pore structure characteristics. As mentioned earlier, the samples needed to be dried to at least 60% RH (at room temperature) in order to minimise the effect of pore saturation on the measured transport coefficients. Therefore, the discs were conditioned by either drying at 55% RH (at 20 °C using saturated $Na_2Cr_2O_7$) or at elevated temperatures of 50 °C and 105 °C until constant mass, taken when the rate of mass loss was not more than 0.01%/d. Some samples were dried at elevated temperatures in order to deliberately induce microcracks. For conditioning at 50 °C, the oven humidity was maintained at 10% by using saturated $ZnCl_2$; this provides about the same vapour density as the vapour density at 55% RH and 20 °C so that a similar equilibrium moisture state was achieved at the end of the conditioning regime. Drying at 105 °C would remove all evaporable water in about 3–14 d. Conditioning at 55% RH (20 °C) required about 6 months while conditioning at 50 °C (10% RH) took about 90 d for the samples to achieve constant mass.

Since the samples were to be transport tested at room temperature, care had to be taken to ensure that the moisture content did not increase when the oven-dried samples were cooled. To ensure this, the oven-dried samples were transferred into a vacuumed desiccator and allowed to cool naturally to room temperature. The discs were taken out of the desiccator only when required for testing. Checks by weighing found negligible mass increase. Discs that were conditioned at RH 55% were wrapped in cling-film for another week to allow for moisture redistribution before transport testing and imaging.

### 2.3. Transport testing

Three replicate discs were tested following the sequence of oxygen diffusion, oxygen permeation and water absorption. All specimens were tested at the same age (30 weeks) and at room temperature. Oxygen diffusivity was determined using the method suggested by Lawrence [10]. The test was carried out by exposing the opposite faces of a disc to a stream of oxygen and nitrogen at the same pressure. The oxygen and nitrogen counter-diffuse through the specimen and the oxygen concentration in the outflow stream was measured to calculate diffusivity. Oxygen permeability was determined by measuring the steady-state flow rate at three input pressures of 0.5, 1.5 and 2.5 bars. The apparent permeability coefficient was calculated following Darcy's equation at each pressure, from which the intrinsic permeability coefficient was determined by Klinkenberg correction [11]. The water absorption test was performed by monitoring mass gain due to capillary absorption with time. Deionised water was used as the test fluid. The mass of absorbed water per unit area of the inflow face was plotted against the square-root of time. A best-fit line was drawn for the first 15 readings (approximately 6 h of measurement) and the slope of this was reported as the sorptivity coefficient. The coefficients of regression of the least-squares fit in the Klinkenberg method and water absorption plot were always greater than 0.99. A detailed explanation of all transport test procedures used is available in Ref. [5].

### 2.4. Backscattered electron imaging

After conditioning, the 10 mm thick discs were sectioned using a diamond saw to produce block specimens (40 × 20 × 10 mm) at approximately mid-distance from the centre to the edge. A non-aqueous solution was used as a lubricating fluid. The blocks were freeze-dried, vacuum-impregnated with a low viscosity epoxy and then ground using silicon carbide papers of successively finer grit size of 220, 500, 1000 and 1200 (68, 30, 18 and 14 μm). The blocks were then polished using cloths embedded with diamond abrasives of sizes 9, 6, 3, 1 and ¼ μm. The grinding and polishing was performed at 70 rpm, with a 7 N force applied onto each specimen. The time spent on each grinding and polishing stage was no longer than 2–4 min to minimise relief. After each stage of polishing, the samples were cleaned ultrasonically in acetone. Finally, the flat-polished specimens were coated with a layer of carbon using an evaporative coater.

A JEOL 5410LV scanning electron microscope fitted with a backscatter electron detector was used for imaging. The microscope was operated at an accelerating voltage of 10 kV and working distance of 10 mm. Twenty images were collected per sample at a magnification of 500x. The images were digitised to 1940 × 1455 pixels, giving a field of view of 240 × 180 μm and a pixel spacing of 0.124 μm. This magnification is commonly used for studying pore structure and was chosen as a compromise between adequate resolution and sampling size. Areas of the microstructure to be imaged were selected randomly so that paste in the vicinity of the aggregate particles, i.e. the interfacial transition zone (ITZ), and bulk paste were both represented. In order to ensure random and unbiased sampling, the microscope stage was programmed to move in a grid fashion, stopping at twenty predefined, equally spaced coordinates. Thus, the frequency of an image containing either the ITZ, bulk paste or both will solely

Table 2
Curing and conditioning regimes

| Mixture | Sample designation | Curing period (d) | Conditioning regime |
|---|---|---|---|
| M 0.7 | M 0.7 (2) 105C | 2 | 105 °C |
| | M 0.7 (2) 50C | 2 | 50 °C at 10% RH |
| | M 0.7 (2) 55RH | 2 | 20 °C at 55% RH |
| | M 0.7 (28) 105C | 28 | 105 °C |
| | M 0.7 (28) 50C | 28 | 50 °C at 10% RH |
| | M 0.7 (28) 55RH | 28 | 20 °C at 55% RH |
| M 0.35 | M 0.35 (2) 105C | 2 | 105 °C |
| | M 0.35 (28) 105C | 28 | 105 °C |
| | M 0.35 (28) 50C | 28 | 50 °C at 10% RH |
| | M 0.35 (28) 55RH | 28 | 20 °C at 55% RH |

depend on the aggregate distribution and volume fraction. Areas near the sample edge were not imaged to avoid sampling mortar that may have been saw-damaged.

### 2.5. Image analysis

BSE images of a mortar sample captured at 500× magnification will most likely contain some fraction of sand particles, which will vary significantly from frame to frame. The sand particles must first be removed from the original image using a segmentation algorithm [12] before thresholding and measurement of the pore phase can be carried out. This is because the aggregate greyscale values overlap with that of the hydrated cement paste and this complicates the thresholding of the pore phase. The sand particles themselves may contain some pores, but since they are relatively impermeable compared to the hydrated cement paste, the aggregate pores should not be measured. Therefore, the sand particles are excluded in the analysis and all measurements on the pore structure are made relative to the cement paste area.

A significant challenge for accurate quantitative microscopy is in the segmentation of the phase of interest. For this study, the pore binary image was produced by grey-level thresholding using a newly developed pore-segmentation algorithm [13]. The upper threshold grey-level for pores was determined from the inflection point of the cumulative brightness histogram of the BSE image. This represents a critical point where a small increment in the threshold value will cause a sudden increase in the thresholded area, a condition termed as *overflow*. Fig. 1 shows how this method is applied. The segmented pores consist of capillaries, cracks and hollow-shells. Air voids and bond failures at the aggregate–paste interface were excluded since the former do not contribute to transport while the latter is an artefact of specimen preparation.

Two important pore-structure parameters that are easily obtained from a 2D image are the porosity and the specific surface. Porosity is the volume fraction of the void phase while specific surface is the internal surface area of the solid-pore interface per unit volume. For a uniform, isotropic and random material, the volume fraction of a particular phase is equivalent to its area fraction observed on a plane section, whereas surface area per unit volume is related to the boundary length per unit area [1,2]. The specific surface, when normalised to the pore volume, is equivalent to the inverse of the hydraulic radius, a parameter that relates to the degree of pore refinement or pore complexity. For two materials having the same porosity, but different specific surface areas, the one that has a higher specific surface will have a larger number of finer pores, and/or a more tortuous boundary. Thus, it would be expected that transport increases with porosity, but decreases with specific surface.

Measuring area and boundary length in a digital image can be an error-prone operation because of the finite pixel size, particularly for small features. When imaged at higher magnification or at a better resolution, more irregularities of the boundary become visible and the measured perimeter and area changes. Monte Carlo simulations [14] showed that for the current microscope set-up and image magnification, measurement errors due to the finite pixel size are not significant for pores larger than 1 μm, but the error increases for smaller pores and becomes substantial (>50%) when the pores are smaller than the electron probe size (~0.1 μm). Also, small features are usually noise generated from image capture and segmentation. To reduce these errors, a size filter was applied on the pore binary image that excludes features smaller than 10 pixels. Hence, the smallest detected pores have an equivalent circular radius of 0.22 μm. Monte Carlo simulations predicted a measurement

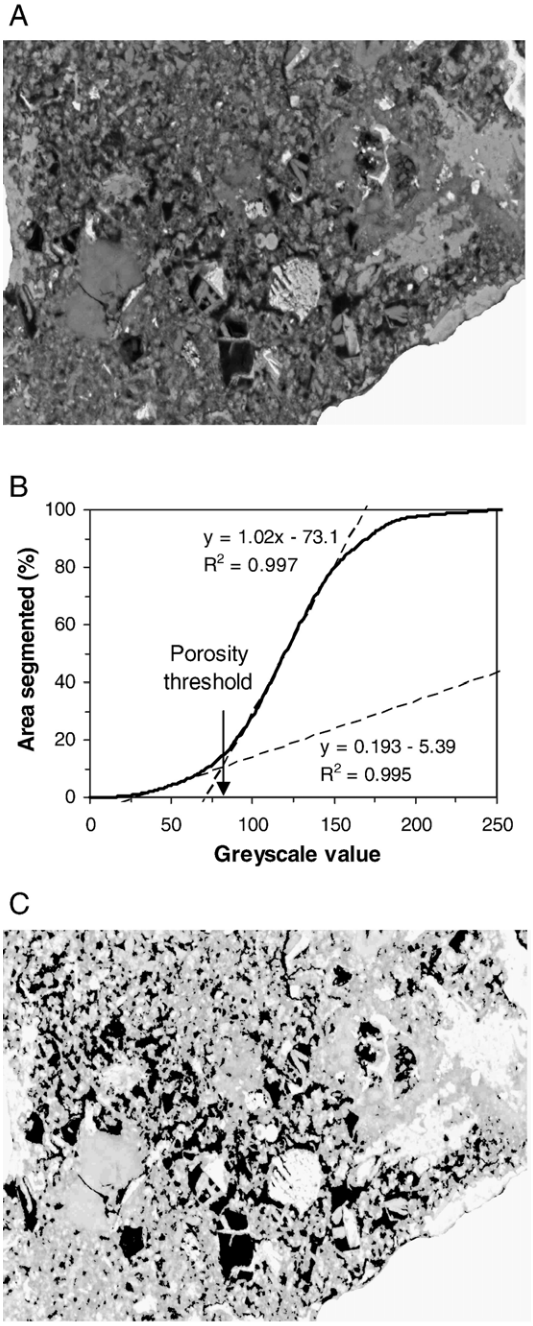

Fig. 1. A) Typical BSE image of M 0.7 (28) 55RH. The aggregate (lower right corner) has been removed from the image. Field of view: 240×180 μm; B) cumulative brightness histogram showing the location of the upper threshold value for porosity; C) segmented pores (black pixels) superimposed onto the original faded BSE image. Pore area fraction is 17.8% of the paste area.

error of about 25% associated with pores at this size, which decreases to ~5% for pores at 1 μm diameter and <1% for pores larger than 5 μm [14].

The porosity ($\Phi_p$), specific surface ($S_p$) and area fraction of unreacted cement particles ($AH_p$) are calculated using Eqs. (1), (2) and (3) respectively.

$$\Phi_p = \frac{\sum A}{\sum A_p} \tag{1}$$

$$S_p = \frac{4}{\pi}\frac{\sum \Gamma}{\sum A} \tag{2}$$

$$AH_p = \frac{\sum A_{AH}}{\sum A_p} \tag{3}$$

where $A$, $A_p$ and $A_{AH}$ are the measured areas of the pores, cement paste and unreacted cement particles, while $\Gamma$ is the measured pore perimeter for each image. Note that the unreacted cement particles were segmented by thresholding the minimum point between peaks in the image greyscale histogram. The porosity and area fraction of the unreacted cement particles are normalised to the paste volume, while the surface area is normalised to the pore volume. We found no significant change in the measured porosity and specific surface area by analysing more than about 20 images (Section 3.1). The unreacted cement area fraction is used to calculate the degree of hydration (α) using the formula $\alpha = 1 - (AH_p/AH_o)$, where $AH_o$ is the volume fraction of the initial cement content normalised to the paste volume fraction, which is 0.31 and 0.47 for M 0.7 and M 0.35 respectively.

## 3. Results

### 3.1. Porosity, specific surface and degree of hydration

Fig. 2 shows the change in the average paste porosity and specific surface with the number of frames analysed. It is observed that a relatively stable value for paste porosity and specific surface can be attained after analysing about twenty images. This suggests that the accuracy of the measurements will not be significantly improved even if more images, taken at the same resolution, were to be analysed.

The average values for paste porosity, specific surface and degree of hydration are given in Table 3. The paste porosity and specific surface range from 8.9 to 33.5% and 2.4 to 5.5 $\mu m^{-1}$ respectively, while the degree of hydration ranges from 0.59 to 0.89. As expected, a lower *w/c* ratio and a longer curing time resulted in lower paste porosity. For samples at the same *w/c* ratio, the paste porosity decreases with increase in degree of hydration. Samples with similar *w/c* ratio and curing age, but conditioned at 55% RH (20 °C) have a slightly higher degree of hydration compared to those conditioned at 50 °C and at 105 °C. Generally, the specific surface increases as the porosity decreases, indicating pore refinement.

It may be instructive to compare the paste porosity and specific surface values measured from image analysis to those obtained via other means. Day and Marsh [15] measured the porosity of various cement pastes cured in saturated limewater using several indirect methods, such as oven drying, resaturation with water, solvent exchange using methanol and propanol, and MIP. The study found that for every sample type, there was a wide range in the porosity values estimated by the various methods. For example, it was observed that a 28-day cured *w/c* 0.71 OPC paste and a 0.30 *w/c* OPC paste had porosity ranging from 49 to 67%, and 20 to 37% respectively. In another study, Cook and Hover [16] used MIP to determine the porosity of OPC pastes cured in saturated limewater at 23 °C. They found that the *w/c* 0.7 pastes had a porosity of 52% (3 d) and 42% (28 d), while the *w/c* 0.3 pastes had a porosity of 22% (3 d) and 17% (28 d). By taking into account the slight differences in *w/c* ratio and curing regimes, the MIP porosity values reported in these earlier studies can be considered to be within a similar range, but are substantially larger than the values obtained in the current study, by a factor of two to three. This discrepancy is not surprising because image analysis only measures a narrow range of pore sizes. Pores smaller than the image resolution are excluded. Also, some large pores may not be counted because these are

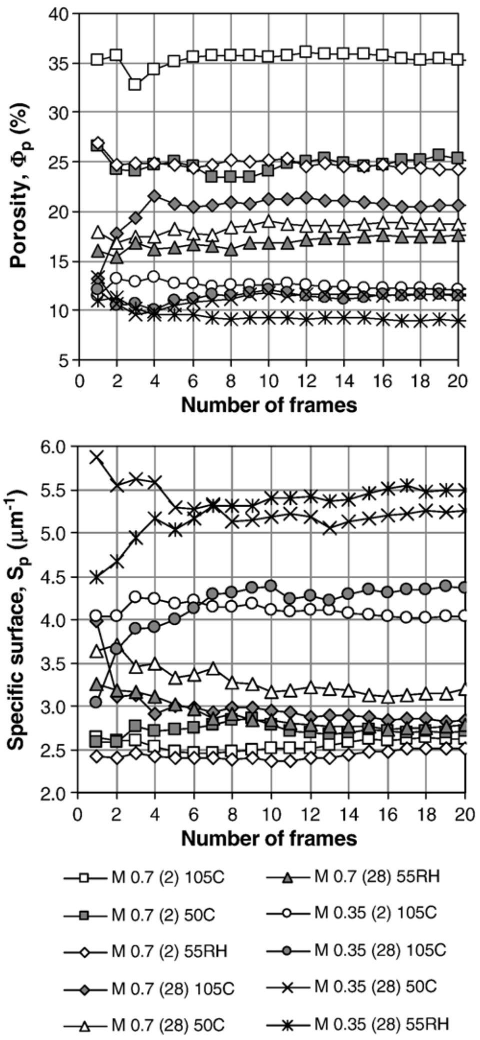

Fig. 2. Variation of average porosity and specific surface with the number of frames analysed. A relatively stable value for porosity and specific surface was obtained after analysing twenty frames.

Table 3
Average values for paste porosity ($\Phi_p$), specific surface ($S_p$), degree of hydration ($\alpha$) and transport coefficients*

| Sample | $\Phi_p$ (%) | $S_p$ ($\mu m^{-1}$) | $\alpha$ | $O_2$ diffusivity ($m^2/s$) | $O_2$ permeability ($m^2$) | Sorptivity ($g/m^2\ min^{0.5}$) |
|---|---|---|---|---|---|---|
| M 0.7 (2) 105C | 33.5 (7.3) | 2.59 (1.4) | 0.59 (1.3) | $6.28\times10^{-7}$ (2.5) | $1.21\times10^{-15}$ (17.7) | 710 (4.8) |
| M 0.7 (2) 50C | 24.6 (1.6) | 2.82 (3.5) | 0.60 (2.5) | $5.82\times10^{-7}$ (8.0) | $8.13\times10^{-16}$ (34.8) | 592 (7.4) |
| M 0.7 (2) 55RH | 24.3 (1.4) | 2.44 (3.9) | 0.68 (1.7) | $5.35\times10^{-7}$ (10.0) | $7.85\times10^{-16}$ (45.2) | 573 (8.3) |
| M 0.7 (28) 105C | 20.6 (0.1) | 2.94 (5.0) | 0.85 (1.1) | $4.36\times10^{-7}$ (10.8) | $4.27\times10^{-16}$ (68.9) | 428 (1.5) |
| M 0.7 (28) 50C | 18.1 (5.7) | 3.32 (7.7) | 0.87 (2.0) | $3.38\times10^{-7}$ (4.8) | $2.47\times10^{-16}$ (15.1) | 314 (3.0) |
| M 0.7 (28) 55RH | 17.6 (0.6) | 2.87 (6.1) | 0.89 (1.2) | $2.64\times10^{-7}$ (9.4) | $3.79\times10^{-16}$ (32.6) | 308 (1.7) |
| M 0.35 (2) 105C | 12.4 (2.3) | 4.06 (0.7) | 0.59 (1.2) | $2.23\times10^{-7}$ (13.4) | $4.12\times10^{-17}$ (53.8) | 205 (1.6) |
| M 0.35 (28) 105C | 11.7 (3.4) | 4.39 (0.6) | 0.71 (1.9) | $1.65\times10^{-7}$ (6.1) | $3.78\times10^{-17}$ (14.7) | 165 (3.5) |
| M 0.35 (28) 50C | 11.3 (3.6) | 5.06 (5.1) | 0.72 (6.6) | $1.16\times10^{-7}$ (5.1) | $2.09\times10^{-17}$ (34.1) | 108 (0.8) |
| M 0.35 (28) 55RH | 8.9 (2.1) | 5.51 (0.3) | 0.74 (3.5) | $3.73\times10^{-8}$ (5.5) | $3.59\times10^{-18}$ (30.7) | 41 (2.1) |

*Values in parentheses represent coefficient of variation (%).

either inadequately sampled due to the image size and number of frames, or are intentionally excluded if it was considered a priori that these are isolated voids having little or no contribution to mass transport (for example air voids). In contrast, indirect methods cover a wider range of pore sizes including (perhaps) gel pores, small capillary pores and large air voids that are less relevant to mass transport.

Comparison between specific surface areas measured by image analysis with other methods such as gas sorption, small angle scattering using neutrons (SANS) or X-rays (SAXS), and nuclear magnetic resonance (NMR) relaxation would lead to an even greater discrepancy. For example, these methods normally give specific surface areas in the region of 50 to 150 $m^2/g$ ($N_2$ sorption), 100 to 200 $m^2/g$ (SANS), 200 to 600 $m^2/g$ (SAXS) and up to as high as 900 $m^2/g$ (NMR) for 28-day cured OPC pastes with *w*/*c* ratios 0.35 to 0.70 [17]. Note that the surface areas are normalised to the weight of D-dried paste. Normalising to the pore volume fraction should give specific surface areas in the region of 200 to 4000 $\mu m^{-1}$, which are about 2 to 3 orders of magnitude greater than the values reported in this study. The extremely high surface area obtained by these methods is because a large fraction of the reported value comes from gel pores in the hydration products, while the surface area contributed by capillary pores is relatively small. In addition, these methods (except for gas sorption) include isolated pores in their surface area measurements, while image analysis only determines the surface area of interconnected pores that are intruded by epoxy from the external surface.

Perhaps, a more appropriate comparison would be against the theoretical capillary porosity value ($\Phi_{cap}$) from the well known Powers' model [18], where $\Phi_{cap}=(w/c-0.36\alpha)/(w/c+0.32)$. The results are plotted in Fig. 3. Although the image porosity includes microcracks and hollow-shells in addition to capillary pores, all the measured porosity values are smaller than the Powers' capillary porosity. The difference ranges from about 15 to 50%, with higher errors associated with samples of higher *w*/*c* ratio. Assuming that Powers' model is correct, the result suggests that many capillary pores are smaller than the image resolution and hence, were not detected. The underestimation could also be due to the fact that image analysis only measures the fraction of interconnected, epoxy-filled pores. Isolated capillary pores cannot be intruded by the epoxy and therefore, are not detected in the BSE images because of lack of atomic contrast [19]. On the contrary, Powers' model accounts for all capillary pores regardless of their connectivity. However, it is odd to find more discrepancy at higher *w*/*c* ratio. For M 0.7, the large deviation from Powers' capillary porosity could be due to bleeding effects, which may have reduced the effective *w*/*c* ratio by the bleed water evaporating from the sample or forming large cavities, so that assigning a *w*/*c* of 0.70 in the Powers' model erroneously overestimates the capillary porosity. The bleed water cavities are irregularly shaped, much like entrapped air voids from poor compaction, and therefore, are not sampled (by intent or otherwise) because these large isolated voids are not likely to make much contribution to transport.

### 3.2. Correlations between transport properties and pore structure

Table 3 shows the average transport coefficients for each sample. The results indicate a reduction in transport coefficients with the measured porosity, consistent with reduction in *w*/*c* ratio and with longer curing age. For similarly cured samples, conditioning at 105 °C is the most severe regime with respect to its adverse effect on the transport coefficients, followed by conditioning at 50 °C (10% RH) and at 20 °C (55% RH). Rapid drying stops the hydration process earlier and this produces a coarser pore structure than it would otherwise. Drying at high temperature also generates high thermal gradients that cause

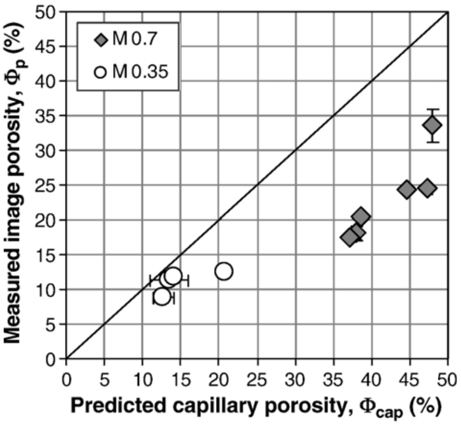

Fig. 3. Comparison between measured paste porosity and theoretical capillary porosity as predicted by Powers' model [18].

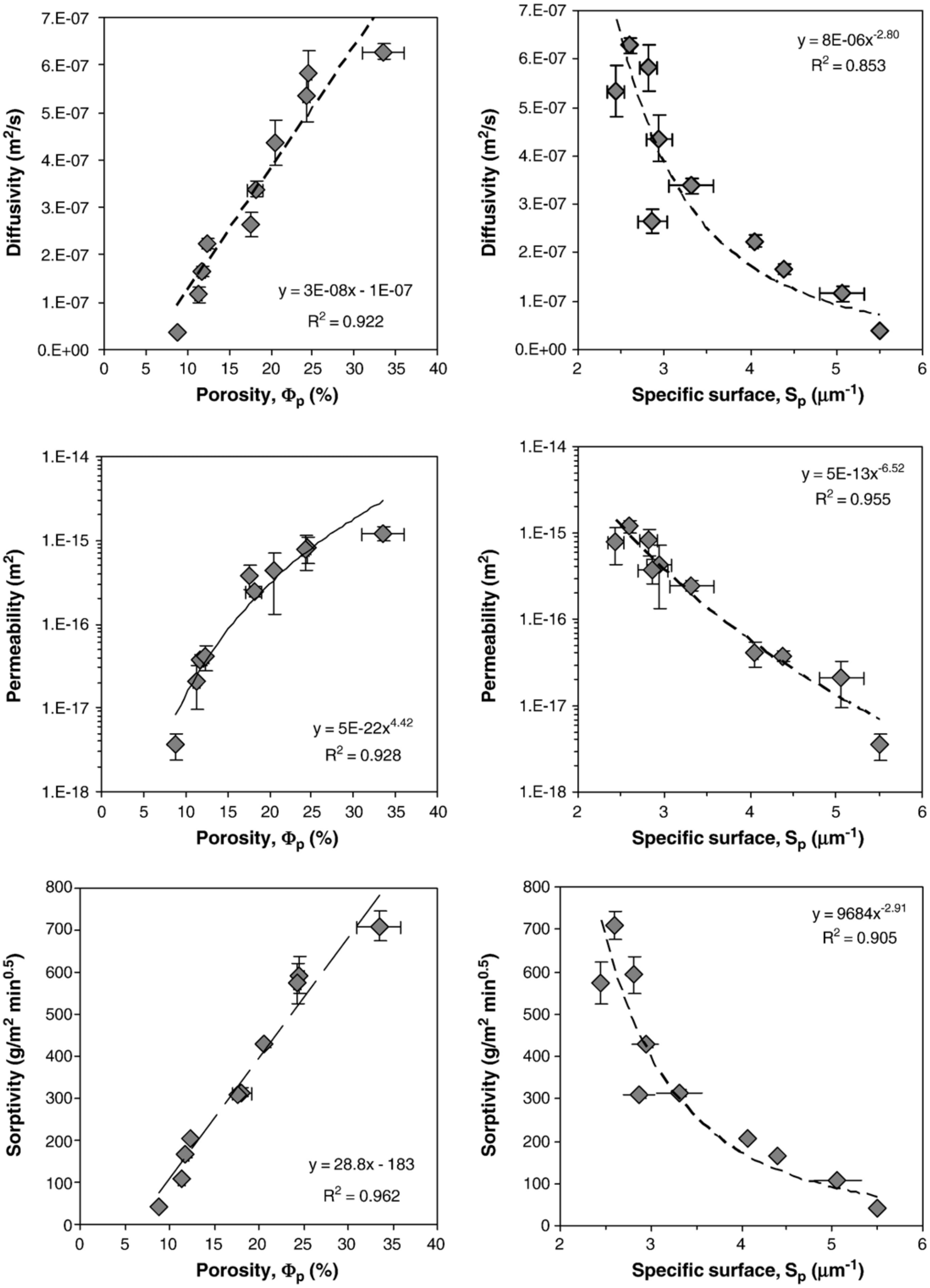

Fig. 4. Relationships between transport coefficients and $\Phi_p$ and $S_p$. Error bars indicate plus–minus one standard deviation. Diffusivity and sorptivity have a positive linear correlation with porosity while permeability is related to porosity by a power function. All three transport properties are correlated to the specific surface by an inverse power function.

microcracking. This is evident in the BSE images of samples conditioned at 105 °C.

When porosity and specific surface are plotted against transport coefficients in Fig. 4, good correlations can be observed. Since the permeability coefficients cover more than 2 orders of magnitude, they were plotted on a logarithmic scale in order to display the data points. The regression lines were obtained using simple curve-fitting to either a linear, power, logarithmic, exponential or polynomial equation, whichever giving the highest coefficient of regression. Both diffusivity and sorptivity are found to have a positive linear correlation with porosity while permeability is related to porosity by a power function. All three transport coefficients are correlated to the specific surface by an inverse power function. The coefficient of regression ($R^2$) is greater than 0.85 in all cases. The results suggest that the detectable image porosity and specific surface have high predictive potentials for transport properties and that they may be used as input values for a pore structure–transport model.

### *3.3. Predicting oxygen diffusivity from porosity, tortuosity and constrictivity*

The effective diffusion coefficient of a non-reactive species in a homogeneous isotropic porous medium, $D$ ($m^2/s$), may be related to its free diffusivity in the absence of the porous material, $D_o$ ($m^2/s$), by the following equation [20]:

$$D = \frac{\delta \Phi}{\tau^2} D_o \tag{4}$$

where $\Phi$ is the porosity, and $\tau$ and $\delta$ are dimensionless parameters accounting for the tortuosity ($\tau \geq 1$) and constrictivity ($0 < \delta \leq 1$) of the porous media. In effect, the above relationship attempts to scale $D_o$ to $D$ by including factors that correct for the reduced available volume for diffusion ($\Phi$), the increased transport path length due to the 'crookedness' of the actual pore channels ($\tau$), and the variation in cross-section of a pore channel over length ($\delta$).

Tortuosity is traditionally defined as the ratio of the effective travel distance through the pore channel to the shortest straight flow path through the medium [21], i.e. $\tau = L_e/L$. In mortars, the tortuosity of the hydrated paste that is formed as a result of the presence of aggregate particles can be used as an initial estimate for the tortuosity of the true transport path. This approach, of course, assumes that because aggregate particles have very much lower porosity than the paste, they act as solid impermeable particles. Using stereology, Stroeven [22] showed that the paste tortuosity is invariant to the aggregate size distribution and can be calculated from the aggregate volume fraction ($V_a$), i.e. $\tau\,(\text{paste}) = 1 + 0.5V_a$. For this study, $V_a = 0.63$, giving a value of 1.315 for the paste tortuosity. We shall use this, but recognise that it is only a lower-bound estimate for the tortuosity of the true transport path. This is because the true tortuosity should equal the paste tortuosity plus the capillary pore tortuosity, i.e. the above equation should, in theory, include a factor ($\geq 1$) representing the 'natural' tortuosity of the capillary pores in a paste specimen (when $V_a = 0$). This factor is unknown, but is expected to be a function of $\Phi$ and approaches unity when porosity is high, i.e. $\lim(\tau) = 1$ when $\Phi \to 1$. For comparison, theoretical modelling based on various random capillary pore network models has produced $\tau$ values of $\sqrt{2}(\approx 1.44)$ [23,24] and $\sqrt{3}(\approx 1.73)$ [25,26]. Other values for tortuosity, for example, $\sqrt{\pi/2}(\approx 1.25)$, have been reported [27].

To estimate the constrictivity factor, the pore channels can be idealised as tubes of circular cross-section with radius that varies in a sinusoidal fashion along the length of the channel, i.e. $r(z) = r_o - \alpha\cos(2\pi z/\lambda)$, where $\alpha$ is the amplitude and $\lambda$ is the wavelength of the radius variation. Constrictivity is then defined as the hydraulic conductance of the sinusoidal pore divided by the hydraulic conductance of a cylindrical pore with an average radius $r_o$. Bernabé and Olson [28] showed that this can be written as a function of the ratio of minimum to maximum pore radius ($r_{min}/r_{max}$) along the sinusoidal pore:

$$\delta = \frac{G}{G_o} = \frac{2\left(1-(\alpha/r_o)^2\right)^{7/2}}{2+3(\alpha/r_o)^2} = \frac{256\rho^{7/2}}{(1+\rho)^4(5\rho^3+3\rho^2+3\rho+5)} \tag{5}$$

where $\rho = (r_o - \alpha)/(r_o + \alpha) = r_{min}/r_{max}$. Therefore, $\delta$ can be obtained from Eq. (5) using a suitable estimate for $r_{min}/r_{max}$. We were unable to measure this from 2D images, so we shall refer to Cargill [29] who reported a value of 0.57 for a pore space formed by a simple cubic arrangement of mono-dispersed spheres and a value 0.29 for a more compact hexagonal packing. The average between these two values will be used, giving a constrictivity factor of 0.44.

The free diffusivity of oxygen in air ($D_o$) is calculated from the Chapman–Enskog equation [30]; at 20 °C and atmospheric pressure, this value is $2.0 \times 10^{-5}$ $m^2/s$. To use Eq. (4) for diffusivity prediction, the paste porosity ($\Phi_p$) has to be converted to sample porosity ($\Phi$) by taking into account the aggregate content, i.e. $\Phi = (1 - V_a)\Phi_p$. Fig. 5 shows the predicted diffusivity plotted against experimental values. The model tends to over-predict for the lower $w/c$ ratio mortar, but the general agreement is reasonable, with 90% of the estimated values within a factor of two, and 100% within a factor of five from the measured values. The vertical bars in Fig. 5 represent the range of predicted diffusivity, should the true value for $\delta$ lie within ±30% of the chosen value (i.e. $\delta$: 0.31–0.57; $\rho$: 0.36–0.50) and for $\tau$, from +0–60% of the chosen value (i.e. $\tau$: 1.315–2.104), hence covering most of the typical values of $\rho$ and $\tau$ reported in the literature. Given such a wide range for $\delta$ and $\tau$, the predicted diffusivities are still within half an order of magnitude from the measured values.

### *3.4. Predicting oxygen permeability using a modified Kozeny–Carman model*

Relations between fluid permeability, porosity and specific surface are generally termed as Kozeny–Carman (K–C) models

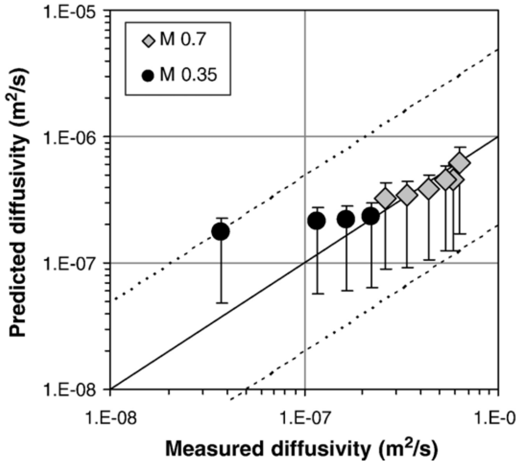

Fig. 5. Predicted and measured values of oxygen diffusivity. 90% of the predicted values were accurate to within a factor of two and 100% to within a factor of five in relation to the measured values.

[31] and these were derived based on hydraulic radius theory for simple pore geometries. The basic example is considering flow, $Q$ ($\mathrm{m}^3/\mathrm{s}$), through a single straight cylindrical tube of radius $r$ (m), which is given by the Hagen–Poiseuille equation $Q = -(\pi r^4/8\eta)(\delta P/\delta z)$, where $\eta$ ($\mathrm{Ns/m}^2$) is the fluid dynamic viscosity and $\delta P/\delta z$ (N/m) is the pressure gradient along the tube. Note that the Hagen–Poiseuille equation is an exact solution of the Navier–Stokes equation for a straight circular tube. For a single cylindrical tube embedded in a block of solid material with cross-sectional area $A$ ($\mathrm{m}^2$), Darcy's law gives $Q = -(kA/\eta)(\delta P/\delta z)$. Thus, by comparing Hagen–Poiseuille's equation with Darcy's law, it follows easily that the effective permeability, $k$ ($\mathrm{m}^2$), is:

$$k = \frac{\pi r^4}{8A} = \frac{\Phi^3}{2s^2} \tag{6}$$

Where the porosity of the sample $\Phi$ is equivalent to $\pi r^2/A$, and the specific surface area, $s$ ($\mathrm{m}^{-1}$), is given by the tube surface area per unit volume of the sample, i.e. $s = 2\pi r/A$. Eq. (6) is the original form of K–C model for the case of smooth-walled cylindrical pores where the tortuosity $\tau$ of the pore channel is 1. Derivation for a sample with $n$ number of non-intersecting parallel cylindrical tubes of a particular radius distribution also yields a similar equation. Berryman and Blair [32] showed that Eq. (5) is also valid for the case of straight tubes with arbitrary ellipsoidal cross-sections. For pores with tortuosity $\tau$, Walsh and Brace [33] showed that:

$$k = \frac{\Phi^3}{2\tau^2 s^2} \tag{7}$$

The above equation assumes that the pores are of constant cross-sections, thus, it is proposed to include a term, $\delta$, to account for the effect of constrictions in the pore throat. Considering that $s = \Phi S_\mathrm{p}$ and $\Phi = (1 - V_\mathrm{a})\Phi_\mathrm{p}$, we then have:

$$k = \frac{(1-V_\mathrm{a})\delta}{2\tau^2}\frac{\Phi_\mathrm{p}}{S_\mathrm{p}^2} \tag{8}$$

Eq. (8) can be interpreted as a relationship between permeability and the average hydraulic radius ($=1/S_\mathrm{p}$), with parameters that scale the permeability of a non-intersecting capillary tube model to include factors for complexity of the actual porous medium. Note that the factor 2 in the denominator is the originally derived shape factor for straight, circular pores. Thus, the tortuosity and constrictivity factors act to transform the circular pore shape factor to a value that is supposedly representative of the actual pore geometry. Provided that $\tau$ and $\delta$ can be estimated realistically, the modified K–C model in the form of Eq. (8) contains no adjustable parameters. Eq. (8) can also be written in a form that involves the formation factor $F$. By taking the analogy between electrical conductivity and diffusion, and referring to Eq. (4):

$$F = \frac{\sigma_\mathrm{o}}{\sigma} = \frac{D_\mathrm{o}}{D} = \frac{\tau^2}{\delta\Phi} \tag{9}$$

Substituting Eq. (9) into Eq. (8) gives:

$$k = \frac{1}{2FS_\mathrm{p}^2} \tag{10}$$

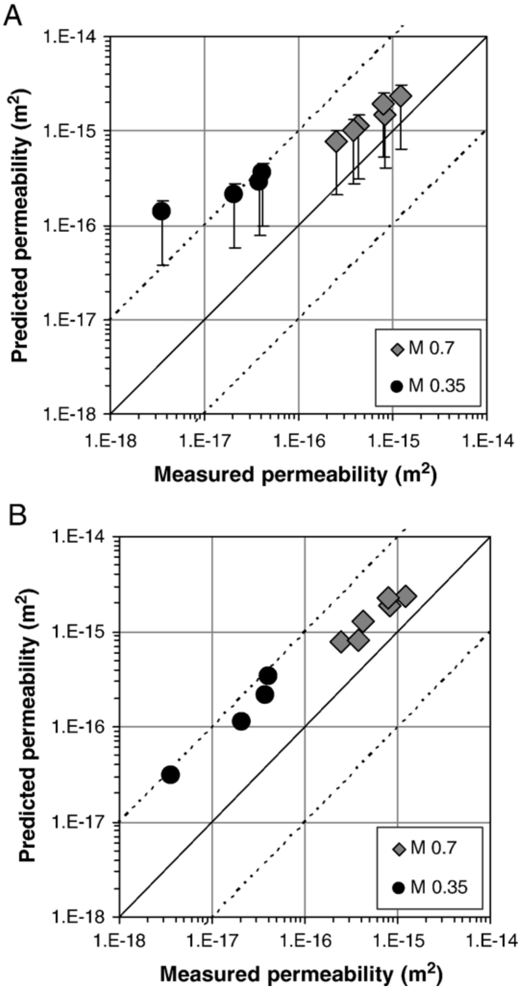

Fig. 6. Predicted and measured values for permeability using: A) Eq. (8) and B) Eq. (10).

Assuming that the pores are saturated with air that is of the same composition as ambient air, the formation factor based on measured oxygen diffusivity ranged from 30 to 530 for all the specimens; this is within the order of values that have been reported previously [34]. Fig. 6 shows the predicted permeability based on Eqs. (8) and (10). The vertical bars in Fig. 6A represent the range of predicted values, given a ±30% error in $\delta$ and +0–60% error in $\tau$. Both equations consistently overpredict with increasing error as the magnitude of permeability decreases. The model incorporating formation factor performed slightly better, with values predicted to within an order of magnitude. This is probably because inclusion of the formation factor in Eq. (10) has improved on the estimated tortuosity and constrictivity values.

## 4. Discussion

As mentioned in the Introduction section, we would like to emphasise that this is an exploratory study of the feasibility of using image-derived pore parameters as inputs to simple analytical models for the prediction of transport properties of cement-based materials. Mortars were chosen for this preliminary study because they resemble concretes by having sand particles and aggregate-paste interfaces, but are more homogeneous by the exclusion of large aggregates. The decision to use very high and low *w*/*c* ratio was based on the intention to study samples of a wide range of pore structure characteristics and to determine the limits of applicability and sensitivity of the derived pore structure-transport relationships. Although only a small number of samples were tested, their transport properties cover a wide range of values (>1 order of magnitude for diffusivity and sorptivity, ~2.5 orders of magnitude for permeability). This reflects on the efficacy of the curing and conditioning regime to produce samples with a range of pore characteristics.

The major assumptions made in this study are: 1) that all pores and cracks segmented from the image are interconnected, 2) the image resolution is sufficient to include all pores contributing to transport and 3) that the pores and microcracks have the same relative importance to transport. The first assumption is reasonable because only pores that are filled with epoxy are visible in a BSE image [19]. Therefore, the segmented pores do not contain any isolated pores. Whilst it is impossible to measure connectivity, we can at least be certain that all the pores tallied from image analysis are connected. However, the second and third assumptions are not strictly valid because features smaller than the resolution limit have not been detected and microcracks may have a higher relative contribution to transport in a severely damaged sample. Nevertheless, the strong correlation obtained between the measured pore properties with transport coefficients and the relatively good prediction obtained shows that the range of pore size analysed is relevant.

The diffusivity and permeability for M 0.35 were consistently over-predicted, with increasing error as the sample porosity decreased. These errors cannot only be explained by measurement errors resulting from the finite pixel size, which are comparatively modest. For example, Monte Carlo simulation [14] predicted a maximum error of about 25% for the smallest pores measured in this study. Thus, using simple error analysis, this only translates to an over-prediction of about 50–100% for diffusivity and permeability. A possible reason for the over-prediction is that at low porosity, the paste tortuosity significantly underestimates the true tortuosity since the actual transport path deviates more from the paste tortuosity as the pores become finer. This could explain why a better prediction was obtained for the higher *w*/*c* sample. Also, fine capillaries that are smaller than the image resolution may have a role in transport and measuring these will increase the specific surface significantly, but will have only a marginal effect on the porosity, therefore the net result would be improved prediction of permeability (see Eqs. (8) and (10)). Another possible reason for the over-prediction could be the influence of hollow-shells. In dense pastes, a large fraction of the observed pores are typically hollow-shells, which are isolated from each other and the degree of connectivity with capillary pores is smaller [35] so transport may be governed only by the capillaries. Therefore, an improvement in the transport prediction is likely to be achieved if hollow-shells are excluded in the analysis for dense pastes.

Although the tortuosity and constrictivity factors used in this study have not been measured directly, it is shown that errors in the estimated values of $\delta$ and $\tau$ do not strongly affect the predictions. 3D imaging techniques, such as laser scanning confocal microscopy [35], are expected to provide valuable information with regards to these, for instance, a better estimate for $r_{\min}/r_{\max}$. The connectivity of the pore structure has been neglected in this study. However, tortuosity should in theory, be very closely related to connectivity; a highly connected pore structure of a random porous material should have a low tortuosity due to shortening of the effective transport path length and vice versa. This suggests that if tortuosity can be accurately determined, the error associated with not having connectivity as a parameter in the model will not be large.

Quenard et al [36] combined the results from mercury porosimetry and BSE imaging with advanced multi-scale computational modelling techniques involving 3D reconstruction from 2D images and renormalisation using a cubic lattice pore network model, to predict vapour diffusivity and air permeability of lime–silica brick, clinker brick and Baumberger sandstone. The transport properties of the materials investigated ranged from $1\times10^{-15}$ m$^2$ to $3.9\times10^{-14}$ m$^2$ for air permeability and $5.6\times10^{-7}$ m$^2$/s to $1.1\times10^{-6}$ m$^2$/s for vapour diffusivity, which correspond to the most porous samples in the present study. The reconstruction technique and subsequent image-based computations by solving Stoke's equation using a finite-difference method and Laplace's equation using a conjugate gradient technique gave computed air permeability and vapour diffusivity within a factor of 2 of the measured values. The renormalisation technique gave permeabilities that were close to measured values (<50% error) but for diffusivity, the discrepancies were much higher, around an order of magnitude. It appears then, that the accuracy of the simple analytical models presented in this study is comparable to the more sophisticated computational models presented by Quenard et al [36]. However, we believe there is still much room for improvement, for example by increasing the image resolution to include finer pores and by using 3D microscopy to obtain better estimates for tortuosity and constrictivity.

## 5. Conclusions

Mortar specimens of a very high and low *w*/*c* ratio were cured and conditioned in several ways to produce specimens with a range of pore structure and transport properties. Using image analysis on backscattered electron images, porosity and specific surface values were determined, and these were found to correlate very well with the measured oxygen diffusivity, oxygen permeability and water sorptivity. This shows that despite the limitations of 2D image analysis, it is still a viable tool for extracting quantitative information of the pore structure that can be used as input values for a transport prediction model. A simple analytical model incorporating tortuosity and constrictivity was used to predict oxygen diffusivity and a variant of the Kozeny–Carman model was used to predict oxygen permeability. To estimate the effect of constrictions on transport properties, the pore channels were idealised as tubes of circular cross-sections of sinusoidally varying radius. For mortars, the paste tortuosity which is a function of aggregate volume content gives a lower-bound estimate of the true transport path tortuosity. It was found that the diffusion model tends to over-predict for the lower *w*/*c* ratio mortar, but the general agreement was reasonable, with 90% of the estimated values within a factor of two from the measured values. The Kozeny–Carman model, however, overpredicted all permeability values with an error of between half to one order of magnitude.

## Acknowledgements

HSW acknowledges the financial support provided by Universities UK, via the Overseas Research Students Awards Scheme. We thank Mr. R. A. Baxter for his help with the laboratory work.

## References

[1] E.E. Underwood, Quantitative Stereology, Addison-Wesley, Reading, Massachusetts, 1970.

[2] J.C. Russ, R.T. Dehoff, Practical Stereology, Second Edition, Plenum Press, New York, 1999.

[3] J. Hu, P. Stroeven, Application of image analysis to assessing critical pore size for permeability prediction of cement paste, Image Anal. Stereol. 22 (2003) 97–103.

[4] M. Koster, J. Hannawald, W. Brameshuber, Simulation of water permeability and water vapour diffusion through hardened cement paste, Comput. Mech. 37 (2) (2006) 163–172.

[5] N.R. Buenfeld, E. Okundi, Effect of cement content on transport in concrete, Mag. Concr. Res. 50 (4) (1998) 339–351.

[6] L.J. Parrott, Moisture conditioning and transport properties of concrete test specimens, Mat. Struct. 27 (1994) 460–468.

[7] J.P. Ollivier, M. Massat, L. Parrott, Parameters influencing transport characteristics, in: J. Kropp, H.K. Hilsdorf (Eds.), Performance Criteria for Concrete Durability, RILEM Report, vol. 12, E & FN Spon, London, 1995, pp. 33–92.

[8] C. Galle, J.F. Daian, M. Pin, Transfert des gaz dans les materiaux, cimentaires: experimentation et modelisation du cauplage microstructure, saturation en eau/permeabilitite, Journee Techniques, AFPC-AFREM, Durabilite des Betons, 1997, pp. 207–219.

[9] F. Jacobs, Permeability to gas of partially saturated concrete, Mag. Concr. Res. 50 (2) (1998) 115–121.

[10] C.D. Lawrence, Transport of oxygen through concrete, in: F.P. Glasser (Ed.), The Chemistry and Chemically-Related Properties of Cement, British Ceramic Society Proceedings, vol. 35, 1984, pp. 277–293.

[11] L.J. Klinkenberg, The Permeability of Porous Media to Liquids and Gasses, Drilling and Production Practice, American Petroleum Institute, New York, 1941, pp. 200–214.

[12] R. Yang, N.R. Buenfeld, Binary segmentation of aggregate in SEM image analysis of concrete, Cem. Concr. Res. 31 (2001) 437–441.

[13] H.S. Wong, M.K. Head, N.R. Buenfeld, Pore segmentation of cement-based materials from backscattered electron images, Cem. Concr. Res. 36 (6) (2006) 1083–1090.

[14] H.S. Wong, N.R. Buenfeld, On the sampling of subsurface material, resolution and measurement errors in quantitative backscattered electron microscopy of the pore structure, Cem. Concr. Res. (in preparation).

[15] R.L. Day, B.K. Marsh, Measurement of porosity in blended cement pastes, Cem. Concr. Res. 18 (1988) 63–73.

[16] R.A. Cook, K.C. Hover, Mercury porosimetry of hardened cement pastes, Cem. Concr. Res. 29 (1999) 933–943.

[17] J.J. Thomas, H.M. Jennings, A.J. Allen, The surface area of hardened cement paste as measured by various techniques, Concr. Sci. Eng. 1 (1999) 45–64.

[18] T.C. Powers, T.L. Brownyard, Studies of the physical properties of hardened Portland cement paste, Bulletin 22, 1948, Research Laboratories of the Portland Cement Association, Skokie, IL, reprinted from J. Am. Concr. Inst., 43 (1947), 101–132, 249–336, 469–505, 549–602, 669–712, 845–880, 933–992.

[19] H.S. Wong, N.R. Buenfeld, Patch microstructure in cement-based materials: Fact or artefact? Cem. Concr. Res. 36 (5) (2006) 990–997.

[20] J. Van Brakel, P.M. Heertjes, Analysis of diffusion in macroporous media in terms of a porosity, a tortuosity and a constrictivity factor, Int. J. Heat Mass Transfer 17 (1974) 1093–1103.

[21] N. Epstein, On tortuosity and the tortuosity factor in flow and diffusion through porous media, Chem. Eng. Sci. 44 (3) (1989) 777–779.

[22] P. Stroeven, A stereological approach to roughness of fracture surfaces and tortuosity of transport paths in concrete, Cem. Concr. Comp. 22 (2000) 331–341.

[23] P.C. Carman, Fluid flow through granular bed, Trans. Inst. Chem. Eng. 15 (1937) 150–156.

[24] E.E. Peterson, Diffusion in a pore of varying cross section, Am. Inst. Chem. Eng. J. 4 (1958) 343–345.

[25] S.K. Bhatia, Directional autocorrelation and the diffusional tortuosity of capillary porous media, J. Catal. 93 (1985) 192–196.

[26] R.C. Dykhuizen, W.H. Casey, An analysis of solute diffusion in rocks, Geochim. Cosmochim. Acta 53 (1989) 2797–2805.

[27] D.P. Haughey, G.S.G. Beveridge, Structural properties of packed beds, Can. J. Chem. Eng. 47 (1969) 130–140.

[28] Y. Bernabé, J.F. Olson, The hydraulic conductance of a capillary with a sinusoidal varying cross-section, Geophys. Res. Lett. 27 (2) (2000) 245–248.

[29] G.S. Cargill, Radial distribution functions and microgeometry of dense random packings of hard spheres, in: D.L. Johnson, P.N. Sen (Eds.), Physics and Chemistry of Porous Media, AIP Conference Proceedings, vol. 107, American Institute of Physics, New York, 1984, pp. 20–36.

[30] W.J. Thompson, Introduction to Transport Phenomena, Prentice Hall Inc, London, 2000.

[31] P.C. Carman, Flow of Gasses Through Porous Media, Academic Press, New York, 1956.

[32] J.G. Berryman, S.C. Blair, Kozeny–Carman relations and image processing methods for estimating Darcy's constant, J. Appl. Phys. 62 (6) (1987) 2221–2227.

[33] J.B. Walsh, W.F. Brace, The effect of pressure on porosity and transport properties of rock, J. Geophys. Res. 89 (1984) 9425–9431.

[34] P.J. Tumidajski, A.S. Schumacher, On the relationship between the formation factor and propan-2-ol diffusivity in mortars, Cem. Concr. Res. 26 (9) (1996) 1301–1306.

[35] M.K. Head, H.S. Wong, N.R. Buenfeld, Characterisation of 'Hadley' grains by confocal microscopy, in: Hughes, et al., (Eds.), 10th Euroseminar on Microscopy Applied to Building Materials, University of Paisley, 2005.

[36] D.A. Quenard, Ke Xu, H.M. Künzel, D.P. Bentz, N.S. Martys, Microstructure and transport properties of porous building materials, Mat. Struct. 31 (1998) 317–324.